

# Predictive 3D modelling of free oblique cutting introducing an ANN-based material flow law with experimental validation over a wide range of conditions

François Ducobu<sup>a,\*</sup>, Olivier Pantalé<sup>b</sup>, Bert Lauwers<sup>c</sup>

<sup>a</sup>*Machine Design and Production Engineering Lab, Research Institute for Science and Material Engineering, UMONS, Belgium*

<sup>b</sup>*Laboratoire Génie de Production, INP/ENIT, Université de Toulouse, Tarbes, France*

<sup>c</sup>*Department of Mechanical Engineering, KU Leuven & Flanders Make@KU Leuven-MaPS, Belgium*

---

## Abstract

Modelling of the cutting process needs to move from 2D to 3D configurations to get closer to industrial applications. This study introduces a predictive 3D finite element model of free orthogonal and oblique cutting with an Artificial Neural Network (ANN)-based material flow law and experimental validation in strictly the same conditions (cutting and geometrical). The flow law based on a neural network allows simulating the cutting process based on data coming from the material characterization tests without requiring any postulate concerning the expression of the flow law. The developments are applied to the formation of continuous chips for the titanium alloy Ti6Al4V and an unseen broad range of 36 cutting conditions is considered: 2 cutting edge inclinations, 3 uncut chip thicknesses and 6 cutting speeds. The predictive performance of the model (i.e., the evaluation of the trends of fundamental variables with the absence of tuning of both numerical parameters and model features when cutting conditions are significantly modified) is high for the forces, mainly cutting and passive, and the chip thickness ratio on all 36 cutting conditions. The accuracy of the main cutting force is excellent: the average difference with the experiments is 4 %, within the experimental dispersion. No significant degradation of the results is brought by the apparition of the third, out-of-plane, force, which shows the ability of the model to handle orthogonal and oblique cutting configurations.

---

\*Corresponding author. Tel.: +32 65 45 68

Email address: [Francois.Ducobu@umons.ac.be](mailto:Francois.Ducobu@umons.ac.be) (François Ducobu)

*Keywords:*

Oblique cutting, Finite element method (FEM), Predictive model, Artificial Neural Network (ANN), Material flow law

---

## 1. Introduction

Selection of the tools and the cutting conditions in machining are still difficult to achieve because of the high level of complexity and the related nonlinear phenomena. Comprehension of the influence of the process parameters on the quality of a component and its optimization are also a challenge for the same reasons. In the frame of digital manufacturing and Industry 4.0, modelling the cutting process supports them, while remaining a challenging task. As highlighted by Arrazola et al. [1], most finite element (FE) models are developed in 2D (orthogonal cutting configuration usually) although industrial applications require 3D modelling.

The behaviour of the machined material is one of the key aspects of a FE model [1, 2]. Research is very intense in this area, leading to a growing number of constitutive material models ranging from empirical models to physical models, some including microstructure effects [2]. The empirical thermo-elasto-viscoplastic Johnson-Cook (JC) model [3] is still the most widely used to this day:

$$\sigma^y = \left( A + B \varepsilon^{p^n} \right) \left( 1 + C \ln \frac{\dot{\varepsilon}^p}{\dot{\varepsilon}_0^p} \right) \left( 1 - \left[ \frac{T - T_{\text{room}}}{T_{\text{melt}} - T_{\text{room}}} \right]^m \right) \quad (1)$$

In this model, the flow stress,  $\sigma^y$ , is a function of the plastic strain,  $\varepsilon^p$ , the plastic strain rate,  $\dot{\varepsilon}^p$ , and the temperature,  $T$ . It is composed of 3 terms describing independently the plastic, viscous and thermal aspects. One of the points in favour of its adoption is the rather limited number of parameters to be identified, 5:  $A$ ,  $B$ ,  $C$ ,  $m$  and  $n$ . Here,  $\dot{\varepsilon}_0^p$  is the reference plastic strain rate, while  $T_{\text{room}}$  and  $T_{\text{melt}}$  are respectively the ambient (room) and melting temperatures. More recent models developed on this basis, such as that of Calamaz et al. [4], increase this number of parameters (for the particular Calamaz model to 9). Other authors have also used Zerilli-Armstrong model to simulate cutting processes [5]. The best description (in theory) of the behaviour is obtained at the cost of a greater complexity of the identification process and a reduction of the link with the physical meaning of the model.

One of the problems of modelling material behaviour for cutting simulation is the identification of parameters, especially as the experimental equipment does not allow the high levels of strain, strain rate and temperature of machining to be

31 achieved [2]. Inverse identification is an alternative, but the uniqueness of the so-  
32 lution is not always guaranteed [1, 2]. Early work by Özel and Altan [6] used the  
33 least squares method to identify the input parameters of a FE model in an inverse  
34 manner. Shrot and Bäker [7] then used the Levenberg-Marquardt algorithm for  
35 their identification of the material parameters. They showed that similar results  
36 (cutting forces and chip morphology) could be obtained by different sets of pa-  
37 rameters and thus highlighted the non-uniqueness of the solution of the inverse  
38 problem. In addition to the flow stress parameters, Klocke et al. [8] also identi-  
39 fied the damage parameters. In more recent work, such as Bosetti et al. [9] and  
40 Denkena et al. [10], the approach to the inverse identification problem is shifting  
41 from optimization to Artificial Intelligence (AI) based methods. The Downhill  
42 Simplex Algorithm (DSA) is adopted by Bergs et al. [11] and by Hardt et al. [12]  
43 for AISI 1045. Stampfer et al. [13] also chose DSA when treating AISI 4140  
44 quenched at 3 different temperatures. In [14], Hardt et al. showed that Parti-  
45 cle Swarm Optimization (PSO) was more efficient in solving the inverse problem  
46 than DSA, even though the computational time is still significant. In order to re-  
47 duce the computational time, an Efficient Global Optimization algorithm (EGO)  
48 was recently introduced by Kugalur Palanisamy et al. [15]. They identified simul-  
49 taneously the parameters of the material constitutive model and the friction model  
50 for Ti6Al4V. The identified parameters showed good performance when applied  
51 to a different FE model [16]. Most of these works highlight the non-uniqueness  
52 of the identification and they all require the definition of the analytical expression  
53 of the constitutive model.

54 ANN (Artificial Neural Network)-based material models have been introduced  
55 to avoid postulating or knowing the analytical expression of the material be-  
56 haviour. Gorji et al [17] recently reviewed the use of recurrent neural networks  
57 for material models, while Jamli and Farid [18] reviewed their application in FE  
58 simulation of material forming. When compared to classical analytical and em-  
59 pirical models, such as JC model, they proved to be more powerful to represent  
60 the experimental behaviour [19]. Use of these ANN-based models in FE simula-  
61 tion of forming processes also turned out to provide better results than the classical  
62 JC model [20] and to handle complex phenomena such as dynamic recrystallisa-  
63 tion [21]. No application of these ANN-based models in FE simulation of cutting  
64 currently exists.

65 Lagrangian and Eulerian formulations are the most used for FE modelling of  
66 the cutting process. Combinations of formulations, such as Arbitrary Lagrangian-  
67 Eulerian (ALE) and Coupled Eulerian-Lagrangian (CEL), are increasingly being  
68 used to avoid (or reduce) mesh distortions [22]. The CEL formulation has recently

been successfully applied to the modelling of cutting (in 2D orthogonal configuration): it provides accurate results with realistic chip shape and no mesh distortion. The first 3D applications are found in recent works [23–27]. They cover orthogonal (free) cutting or a simple 3D operation, while free oblique cutting has yet to be studied.

Experimental validation of a model is a crucial step in modelling the cutting process. The experimental configuration should be as close as possible to the simulation. For the validation of orthogonal cutting, a rotational motion usually generates the cutting speed. This is often done in turning [28] or milling [23] and the diameter of the rotating workpiece must be large enough to reduce the influence of curvature on the results. Experimental configurations under strictly orthogonal cutting conditions are less often adopted, for example on broaching machines [29] or milling machines [30, 31]. If they remove the assumptions related to the rotary cutting motion, they generally allow lower cutting speeds (except on a dedicated machine, as in Afrasiabi et al. [32]). Free oblique cutting with a straight cutting edge has not yet been studied: all efforts have been concentrated on orthogonal cutting (mainly for validation of 2D FE models).

This paper fills the gap in the oblique cutting literature by investigating both orthogonal and free oblique 3D cutting configurations, both experimentally and numerically. An ANN, introduced in Pantalé et al. [33], is implemented in a FE cutting model for the first time in place of the JC analytical law. A wide range of cutting speeds (6), uncut chip thicknesses (3) and cutting edge inclination angles (2) resulting in 36 different conditions are considered to demonstrate the predictive capability of the FE model for the fundamental variables. The developments are applied to the formation of continuous chips of the titanium alloy Ti6Al4V.

## 2. Experimental setup

A 3-axis GF Mikron VCE 600 Pro milling machine is used to perform dry orthogonal and oblique cutting tests on Ti6Al4V (grade 5 annealed at 750 °C for 1 h followed by air cooling) with the same kinematics as a shaper. As shown in Figure 1, the tungsten carbide tool (modified LCGN160602-0600-FG, CP500 from SECO) is fixed on a dedicated holder (modified CFHN-06 from SECO) and the sample to be cut is clamped in the spindle (no rotation is allowed during the test). The top of the sample has 3 ribs of 1 mm width (the width of the tool is 6 mm) and 10 mm length. The test consists of removing the top layer (its height is the uncut chip thickness,  $h$ ) of a rib at the prescribed cutting speed,  $v_c$ . The cutting speed is provided by the feed rate,  $v_f$ , of the machine (maximum value of

105 40 m/min). The tool cutting edge inclination,  $\lambda_s$ , results from the relative angular  
 106 orientation of the tool and the sample. Table 1 shows the cutting conditions: 6  
 107 cutting speeds, 3 uncut chip thicknesses and 2 inclination angles, each repeated  
 108 3 times. [FD:] Add comment to link with SECO's recommendations for the  
 109 standard tool + reference

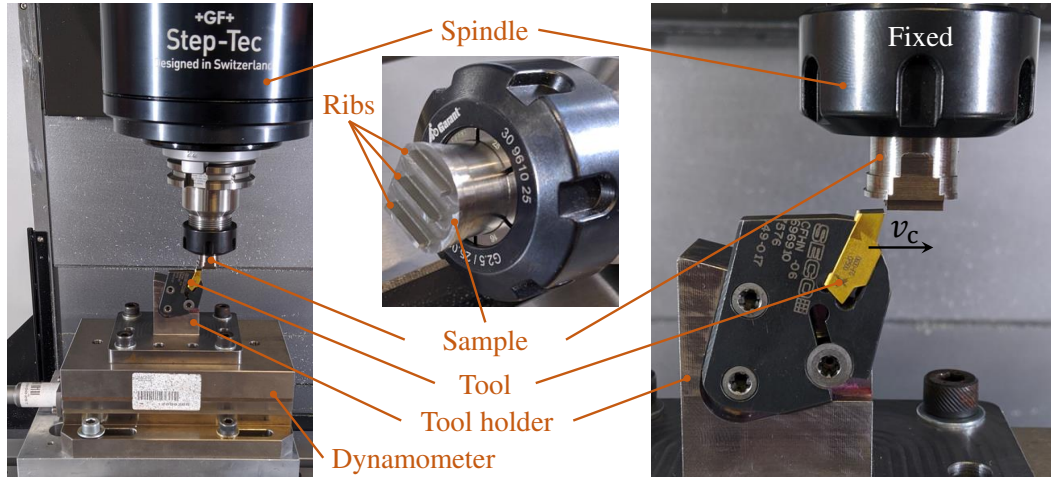


Figure 1: Experimental setup

Table 1: Cutting conditions of the study

Parameter	Values
Cutting speed, $v_c$ (m/min)	5, 7.5, 10, 20, 30, 40
Uncut chip thickness, $h$ ( $\mu\text{m}$ )	40, 60, 80
Cutting edge inclination, $\lambda_s$ ( $^\circ$ )	0, 6
Width of the workpiece (mm)	1
Length of the workpiece (mm)	10
Width of the cutting edge (mm)	6 (1.1 in the model)
Cutting edge radius, $r_\beta$ ( $\mu\text{m}$ )	20
Rake angle, $\gamma_0$ ( $^\circ$ )	15
Clearance angle, $\alpha_0$ ( $^\circ$ )	2

110 Forces are measured with a 3-component Kistler 9257B dynamometer and  
 111 are amplified by a Kistler 5070A charge amplifier. Acquisition is performed at

112 3 kHz using a Kistler 5697A2 data acquisition system and DynoWare software.  
113 The recorded forces are then filtered with a second-order low-pass Bessel filter at  
114 750 Hz before calculating the average value of the steady state signal.

115 All chips are collected and observed with a Dino Lite digital microscope  
116 AM7013MZT (5 MP, magnification 20× – 250×). Each chip is measured 3 times  
117 along its length in order to obtain an average value representative of the whole  
118 chip.

### 119 **3. Finite element model**

#### 120 *3.1. Modelling choices*

121 The main objectives of a predictive model are the accurate modelling of trends  
122 in results as conditions change and the good agreement of predicted values with  
123 experimental values (exact values are not expected due to experimental disper-  
124 sions of at least 10 % around the mean values). This type of model is intended to  
125 support future choices and developments without the need for experimental data.  
126 No assumptions are made about the geometry of the workpiece in the model (i.e.,  
127 its width is the same as in experiments), while keeping the calculation time rel-  
128 evant for industrial applications. The CEL formulation is adopted to model the  
129 dry orthogonal and free oblique cutting tests with Abaqus/Explicit 2020. The  
130 3D model is composed of a fixed Lagrangian tool and a Eulerian part (Figure 2).  
131 Chip formation occurs by plastic flow through the Eulerian domain without mesh  
132 distortion. The Eulerian formulation allows for chip formation without damage  
133 properties, by removing modelling assumptions. These two features contribute to  
134 the cutting models providing accurate results and realistic chips [22].

135 As shown in Figure 3, the full width of the workpiece (1 mm), i.e., one rib  
136 in the experiments, is modelled. To allow for chip formation and lateral flow,  
137 the Eulerian domain is wider (it includes the volume in which the material can  
138 move). The volume above the initial part is also meshed with Eulerian elements  
139 for the same reasons. As in the experiments and to satisfy the assumption of  
140 an orthogonal and oblique free cut, the tool is wider than the workpiece (it is  
141 1.1 mm in the model and 6 mm in the experiments). It is very important to note  
142 that the models are the same for both inclination angles: they differ only in the  
143 rotation of the tool by 6° around the Y axis as in the experiments (Figure 3). This,  
144 together with the absence of assumptions when developing the models, contributes  
145 to make the models predictive: no input is changed when the cutting conditions  
146 are changed.

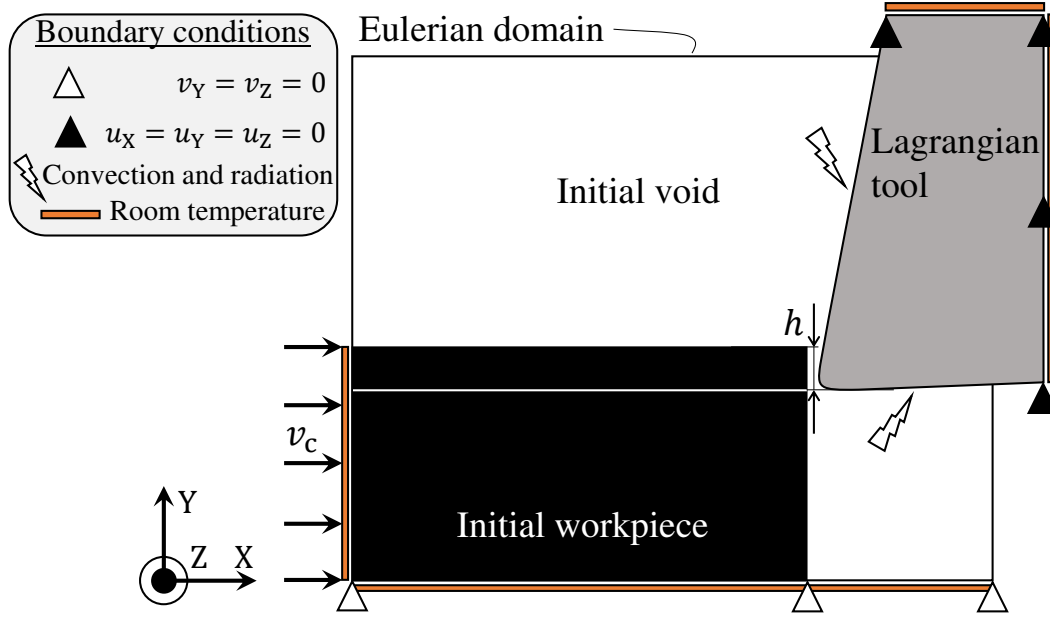


Figure 2: Boundary conditions and schematic initial geometry of the model

147 According to a previous sensitivity study of the mesh in orthogonal cutting  
 148 with the CEL formulation [24], the edge size of the elements is  $5\mu\text{m}$  in the  
 149 plane parallel to the cutting speed. In the direction perpendicular to this plane,  
 150 it is  $5\mu\text{m}$  in the areas close to the lateral boundaries of the Eulerian domain  
 151 and  $50\mu\text{m}$  in the middle of the part. To reduce the computation time, the size  
 152 of the model depends on the value of the uncut chip thickness. This results  
 153 in a Eulerian domain (EC3D8RT 8-node 3D linear Eulerian elements, coupled  
 154 mechanical-thermal behaviour and reduced integration) composed of 216 550 to  
 155 273 350 nodes and a Lagrangian domain (C3D8T 8-node 3D linear Lagrangian  
 156 elements, coupled mechanical-thermal behaviour) of 4650 nodes.

157 The Ti6Al4V part is assumed to be thermo-elasto-viscoplastic (isotropic) and  
 158 the inelastic thermal fraction is 0.9. The JC parameters set of Seo et al. [34]  
 159 is adopted because the value of  $A$  corresponds to the value of the typical yield  
 160 strength of Ti6Al4V and this set was found to provide the best results among the  
 161 20 sets available in the literature [35]. The TiN coated tungsten carbide (WC) tool  
 162 is assumed to have linear elasticity. The material properties are given in Table 2.

163 According to the experimental results of Rech et al. [38], it is assumed that  
 164 Coulomb friction occurs at the tool-piece interface and that the coefficients of

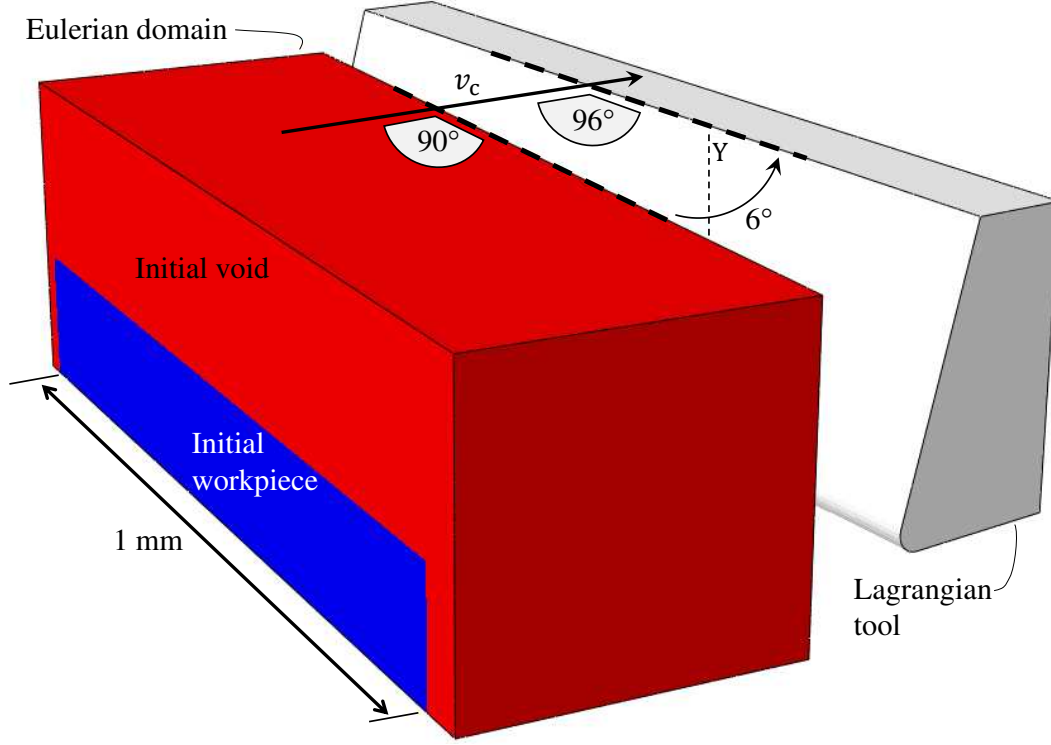


Figure 3: Configuration of the FE model for  $\lambda_s = 6^\circ$

friction,  $\mu$ , and heat partition,  $\beta$ , depend on the cutting speed. The limiting shear stress,  $\tau_{\max}$ , is included and is given by:

$$\tau_{\max} = \frac{\text{yield stress}}{\sqrt{3}} = \frac{A}{\sqrt{3}} \quad (2)$$

All the friction energy is converted into heat. Table 3 shows the friction coefficients adopted in this study.

An ambient temperature of 293 K is imposed on the top and right surfaces of the tool and on the left and bottom surfaces of the workpiece (Figure 2). It is assumed that radiation and convection occur on the rake and clearance faces of the tool. The initial temperature of the tool and workpiece is set to the room temperature (293 K). The heat transfer coefficients are provided in Table 3.

### 3.2. Material model of Ti6Al4V

The material model of Ti6Al4V used in all the numerical simulations proposed in the section 4 is a thermo-elasto-viscoplastic law using a flow criterion



Table 2: Materials properties [34, 36, 37]

Young's modulus, $E$ (GPa)	Ti6Al4V	113.8 <sup>†</sup>
	WC	650
Poisson's ratio, $\nu$	Ti6Al4V	0.34
	WC	0.2
Density, $\rho$ (kg/m <sup>3</sup> )	Ti6Al4V	4430
	WC	14 850
Conductivity, $k$ (W/m K)	Ti6Al4V	6.3 <sup>†</sup>
	WC	100
Expansion, $\alpha$ (1/K)	Ti6Al4V	8.6E−6 <sup>†</sup>
	WC	5E−6
Specific heat, $c_p$ (J/kg K)	Ti6Al4V	531 <sup>†</sup>
	WC	202
JC flow stress	$A$ (MPa)	997.9
	$B$ (MPa)	653.1
	$C$	0.0198
	$m$	0.7
	$n$	0.45
	$\dot{\epsilon}_0$ (1/s)	1
	$T_{\text{room}}$ (K)	293
	$T_{\text{melt}}$ (K)	1873

<sup>†</sup>: Dependence on the temperature, value provided at 293 K

177 based on an Artificial Neural Network (ANN) identified for the chosen material  
178 and implemented in the Abaqus/Explicit code via a Fortran subroutine VUHARD  
179 as proposed by Pantalé et al. in [33]. The principle of this approach consists in  
180 replacing the analytical formulation of the flow law, based on a Johnson-Cook or  
181 Zerilli-Armstrong type model, and allowing the calculation of the flow stress  $\sigma^y$   
182 as a function of the plastic strain  $\epsilon^p$ , the plastic strain rate,  $\dot{\epsilon}^p$ , and the temperature  
183  $T$ , by a multi-layer ANN serving as universal approximator. Thus, the parameters  
184 of the neural network can be directly identified from the experimental data with-  
185 out having to postulate a behavioural model, which simplifies the procedure and  
186 allows greater flexibility in the definition of the model. The proposed approach  
187 also allows, as shown in Pantalé et al. [33], to compute the three derivatives of the  
188 flow stress  $\sigma^y$  with respect to the three input variables of the model, a necessary  
189 step to implement this model as a flow law in the form of a VUHARD subroutine

Table 3: Friction and heat transfer coefficients [36, 38]

Cutting speed, $v_c$ (m/min)	$\mu$	$\beta$
5	0.24	1
7.5	0.22	0.89
10	0.21	0.80
20	0.19	0.63
30	0.18	0.55
40	0.17	0.50
Limiting shear stress, $\tau_{\max}$ (MPa)	576	
Convection, $U$ (W/m <sup>2</sup> K)	50	
Radiation, $\epsilon$	0.3	

190 in the FEM code Abaqus/Explicit, using the exact same network architecture and  
 191 identified trained parameters as the one used to compute the flow stress  $\sigma^y$ .

192 In order to verify the influence of the neural network complexity on the nu-  
 193 merical results of the simulation and on the computation time, several ANN archi-  
 194 tectures are tested afterwards (in 3.4). The chosen global architecture has 2 hidden  
 195 layers with a variable number of neurons for the first hidden layer ( $\zeta = 9$  to 17)  
 196 and 7 neurons for the second hidden layer, 3 inputs (the plastic strain,  $\varepsilon^p$ , the plas-  
 197 tic strain rate,  $\dot{\varepsilon}^p$ , and the temperature,  $T$ ) and one output (the yield strength,  $\sigma^y$ ).  
 198 The global architecture of this type of ANN is given in Figure 4 for 9 neurons in  
 199 the first hidden layer. According to Pantalé et al. [33], this ANN is referred to as  
 200 ANN 3-9-7-1-sig, as it has 3 inputs, 9 neurons in the first hidden layer, 7 neurons  
 201 in the second hidden layer, 1 output and a sigmoid activation function.

202 In a preliminary phase, after having selected the global architecture of the neu-  
 203 ral network, it is necessary to proceed to its training from some inputs. The inputs  
 204 for this application were generated from the Johnson-Cook flow law expression  
 205 reported in Equation (1) and the identified parameters reported in Table 2. This  
 206 approach was chosen to demonstrate the ability of the neural network flow law to  
 207 replace a classically formulated flow law such as Johnson-Cook's for the simu-  
 208 lation of metal cutting. In future developments, experimental tests on a Gleeble  
 209 thermomechanical simulator will be used to generate this network training data.  
 210 The training data, presented in the form of a data table containing the plastic strain  
 211  $\varepsilon^p$ , the plastic strain rate  $\dot{\varepsilon}^p$ , the temperature  $T$  and the flow stress  $\sigma^y$ , is processed

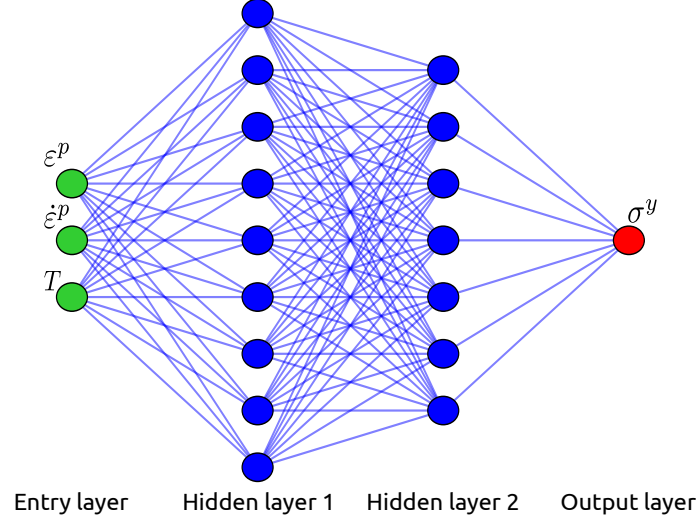


Figure 4: Architecture of the ANN 3-9-7-1-sig used for the flow law

212 by a learning algorithm, developed at LGP, in Python, using the Tensorflow li-  
 213 brary. One hour of training on a Dell XPS13 7390 laptop running Ubuntu 20.04  
 214 64 bits with 16 GiB of Ram and an Intel 4-core i7-10510U processor allow ob-  
 215 taining the converged parameters of the ANN model.

216 Once this learning phase is completed, the neural network parameters result-  
 217 ing from the learning process are used directly by a Python program, in charge  
 218 of automatically generating the Fortran source code of the VUHARD subroutine  
 219 in order to compute the flow stress  $\sigma^y$  and its three derivatives, required for the  
 220 explicit Abaqus FEM code.

221 The main advantage of this approach (the use of an ANN), after the learning  
 222 phase, is that, for example, the output  $\sigma^y$  of the network is now linked to the inputs  
 223  $\varepsilon^p$ ,  $\dot{\varepsilon}^p$ , and  $T$  by the equations (3) to (7) for a two hidden layers neural network  
 224 with a sigmoid activation function as proposed previously.

225 Thus, in the VUHARD subroutine, the computation of the flow stress  $\sigma^y$  from  
 226 the 3 input variables  $\varepsilon^p$ ,  $\dot{\varepsilon}^p$ , and  $T$  is performed using the following procedure.  
 227 The first step is to scale the input data to the interval  $[0, 1]$  using the following  
 228 equation:

$$\vec{x} = \begin{cases} x_1 = \frac{\varepsilon^p - [\varepsilon^p]_{min}}{[\varepsilon^p]_{max} - [\varepsilon^p]_{min}} \\ x_2 = \frac{\ln(\dot{\varepsilon}^p) - [\ln(\dot{\varepsilon}^p)]_{min}}{[\ln(\dot{\varepsilon}^p)]_{max} - [\ln(\dot{\varepsilon}^p)]_{min}} \\ x_3 = \frac{T - [T]_{min}}{[T]_{max} - [T]_{min}} \end{cases} \quad (3)$$

where quantities  $[ ]_{min}$  and  $[ ]_{max}$  are the boundaries of the range of the corresponding field during the training phase. Corresponding values, for the proposed case, are given in Appendix A. According to the architecture of the network, the outputs of the neurons of the first hidden layer  $\vec{y}_1$  are given by the following equation:

$$\vec{y}_1 = \text{sig}\left(\mathbf{w}_1 \cdot \vec{x} + \vec{b}_1\right) \quad (4)$$

where,  $\mathbf{w}_1$  and  $\vec{b}_1$  are the weights and biases associated with the first hidden layer and  $\text{sig}()$  is the sigmoid activation function defined by the equation (5) :

$$\text{sig}(x) = \frac{1}{1 + e^{-x}} \quad (5)$$

Then, the output of the neurons of the second hidden layer is given by the equation (6) :

$$\vec{y}_2 = \text{sig}\left(\mathbf{w}_2 \cdot \vec{y}_1 + \vec{b}_2\right) \quad (6)$$

where,  $\mathbf{w}_2$  and  $\vec{b}_2$  are the weights and biases associated with the second hidden layer. Finally, the  $\sigma^y$  output of the ANN is thus given by the equation (7) :

$$\sigma^y = ([\sigma^y]_{max} - [\sigma^y]_{min})\left(\vec{w}^T \cdot \vec{y}_2 + b\right) + [\sigma^y]_{min} \quad (7)$$

where,  $\vec{w}$  and  $b$  are the weights and the bias associated with the output layer.

On the other hand, the three derivatives of the yield stress  $\sigma^y$  with respect to the three input variables  $\varepsilon^p$ ,  $\dot{\varepsilon}^p$ , and  $T$  are given by the equation (8):

$$\begin{cases} \partial\sigma^y/\partial\varepsilon^p = s'_1 \frac{[\sigma^y]_{max} - [\sigma^y]_{min}}{[\varepsilon^p]_{max} - [\varepsilon^p]_{min}} \\ \partial\sigma^y/\partial\dot{\varepsilon}^p = s'_2 \frac{[\sigma^y]_{max} - [\sigma^y]_{min}}{[\dot{\varepsilon}^p]_{max} - [\dot{\varepsilon}^p]_{min}} \\ \partial\sigma^y/\partial T = s'_3 \frac{[\sigma^y]_{max} - [\sigma^y]_{min}}{[T]_{max} - [T]_{min}} \end{cases} \quad (8)$$

where  $s'_i$  is the  $i^{th}$  component of the vector  $\vec{s}'$  defined by the equation (9):

$$\vec{s}' = \mathbf{w}_1^T \cdot \left[ \mathbf{w}_2^T \cdot \left( \frac{\vec{w} \circ e^{-\vec{y}_2}}{[1 + e^{-\vec{y}_2}]^2} \right) \circ \left( \frac{e^{-\vec{y}_1}}{[1 + e^{-\vec{y}_1}]^2} \right) \right] \quad (9)$$

and  $\circ$  is the elements-wise product, known as the Hadamard product. In equations (3) to (9), quantities  $\mathbf{w}_1$ ,  $\mathbf{w}_2$ ,  $\vec{w}$ ,  $\vec{b}_1$ ,  $\vec{b}_2$  and  $b$  are evaluated by the training

246 procedure of the ANN. Corresponding values for an ANN containing 9 neurons  
 247 in the first hidden layer and 7 neurons in the second hidden layer are reported in  
 248 Appendix A. The set of equations (3) to (9), together with the network param-  
 249 eters identified in the learning phase, is automatically translated into a VUHARD  
 250 Fortran subroutine used by the FEM code Abaqus to simulate the cutting model.

251 Because of the large number of identified parameters for all the ANN models  
 252 (from 114 to 202 for 9 and 17 neurons for the first hidden layer, respectively), the  
 253 other 4 sets of ANN parameters used in this publication can be found in [39].

### 254 3.3. Sensitivity study of the results to mass scaling

255 FE modelling of the cutting process is very expensive in terms of CPU time  
 256 due to the coupling of many nonlinear phenomena and the large amount of tiny  
 257 finite elements. Mass scaling (MS) is introduced into the model to reduce the CPU  
 258 computation time while checking that it does not influence the results (forces and  
 259 energies) via a mass scaling sensitivity study. MS factors,  $MS_f$ , ranging from  
 260 1E6 (theoretical CPU time scale of  $\sqrt{MS_f} = 1000$ ) to 1 (no scale) were used for  
 261 a cutting condition ( $\lambda_s = 0^\circ$ ,  $v_c = 30$  m/min and  $h = 60$   $\mu$ m). The same signal  
 262 processing procedure is applied to the numerical forces as to the experimental  
 263 forces (cf. 2): they are filtered with a second-order low-pass Bessel filter at 750 Hz  
 264 before calculating the steady state average value. Table 4 gives the results of the  
 265 model with MS normalized ( $\hat{F}_i$ ) by those of the model without MS:

$$\hat{F}_i = \frac{F_i \text{ with MS}}{F_i \text{ without MS}} \quad (10)$$

266 with  $i = c$  for the cutting force and  $i = f$  for the feed force. As expected, the  
 267 real speed-up does not increase linearly with the  $MS_f$ , but it remains significant.  
 268 A  $MS_f$  of 1E6 leads to an unstable computation and a  $MS_f$  of 1E5 leads to erratic  
 269 force evolutions. These results are confirmed by high values of the ratio of the  
 270 kinetic ( $KE$ ) to the internal ( $IE$ ) energies (it should not exceed a few % [40, 41]).  
 271 A value of  $MS_f$  of 1E3 is chosen as it offers a good balance between reducing the  
 272 computation time and the impact on the forces, while keeping the  $\frac{KE}{IE}$  below 1 %.  
 273 To provide an order of magnitude of CPU computation time, between 10 h and  
 274 50 h (depending on the value of  $h$ ) are required on 4 cores of an Intel i7-5700HQ  
 275 CPU at 2.7–3.5 GHz.

### 276 3.4. Sensitivity study of the results to the number of neurons

277 The number of neurons in the hidden layers may influence the results. A  
 278 sensitivity study on the number of neurons of the first hidden layer,  $\zeta$ , is performed

Table 4: MS sensitivity study (selected MS factor,  $MS_f$ , in bold,  $\hat{F}_c$ : normalized cutting force,  $\hat{F}_f$ : normalized feed force,  $KE$ : kinetic energy,  $IE$ : internal energy)

$MS_f$	CPU scaling	Speed-up	$\hat{F}_c$	$\hat{F}_f$	$\frac{KE}{IE}$ (%)
1	1	1	1	1	2.3E−4
1E2	10	9	1.006	0.982	2.2E−2
<b>1E3</b>	<b>32</b>	<b>21</b>	<b>1.008</b>	<b>0.940</b>	<b>2.2E−1</b>
1E4	100	61	1.012	0.921	2.4
1E5	316	173	Erratic	Erratic	22
1E6	1000	207	Unstable	Unstable	58

in order to select the ANN offering the best balance between CPU computation time and quality of the results. The results of the study are provided in Table 5.  $\check{F}_i$  corresponds to the results of the model with ANN normalized by those of the model with the built-in JC model:

$$\check{F}_i = \frac{F_i \text{ with ANN}}{F_i \text{ with JC}} \quad (11)$$

They show no influence on the numerical results for the forces compared to the built-in Johnson-Cook model, only the computation time is influenced by the number of neurons in the first hidden layer and increases with it. This increase in computation time is not only due to the increasing complexity of the neural network with the number of neurons, but also to the need to go through a VUHARD user subroutine. A first hidden layer of 9 neurons is therefore selected as it leads to the smallest increase in CPU computation time, without influence on the final result.

#### 4. Experimental and numerical results

An example of the temporal evolution of the numerical and experimental forces is plotted for the 3 directions in Figure 5 at  $\lambda_s = 6^\circ$ ,  $v_c = 10$  m/min and  $h = 40$  m/min. The FE models are calculated up to a few microseconds after the stationary state is reached. Then, a linear extrapolation (dashed line between the last two markers in Figure 5) is used to provide numerical values for the same time range as the experimental values. The average and standard deviation ( $2\sigma$ ) are calculated from the 3 experimental values. The resulting dispersion is shown in Figure 5 around the average values of each force. Steady state takes longer to

Table 5: Sensitivity of the forces to the number of neurons of the first layer,  $\zeta$  (selection in bold,  $\check{F}_c$ : normalized cutting force,  $\check{F}_f$ : normalized feed force)

$\zeta$	Time increase (%)	$\check{F}_c$	$\check{F}_f$
Built-in	0	1.000	1.000
<b>9</b>	<b>6</b>	<b>1.000</b>	<b>0.999</b>
11	6	1.001	1.000
13	7	1.000	0.998
15	8	1.001	1.001
17	10	1.000	1.000

be reached for the experiments than for the numerical model, in particular for the cutting force. The dispersion around the evolution of the average force is greater for the feed force than for the cutting force, while the average value of the feed force is 46 % of the average value of the cutting force. The numerical cutting force is very close to the experimental average cutting force; it is only 4 % higher. This difference,  $\Delta j$ , is calculated by :

$$\Delta j = \frac{|j^{(\text{sim})} - j^{(\text{exp})}|}{j^{(\text{exp})}} \times 100 \quad (12)$$

where  $j$  is the cutting force, the feed force, the passive force or the chip thickness.  $j^{(\text{sim})}$  is the average value from the simulation, while  $j^{(\text{exp})}$  is the average experimental value.

The numerical feed force is underestimated by the model, but is within the 95 % experimental confidence interval. The numerical passive force difference is also underestimated and is not within the narrower experimental dispersion. The difference between the average values of the experimental and numerical feed and passive forces is 25 %. A less well modelled feed force than the cutting force is typical of FE models of the cutting process and the difference with the experimental value is similar to other studies for a narrower range of cutting conditions [32, 42–45]. Hardt and Bergs [27] also obtained larger differences for feed and passive force than for cutting force. The difference for passive force was higher than for feed force, which is the opposite observation of this work.

Numerical chips at  $v_c = 10$  m/min and  $h = 40$   $\mu$ m for  $\lambda_s = 0^\circ$  and  $\lambda_s = 6^\circ$  are provided in Figures 6 and 7. When the inclination of the cutting edge is  $0^\circ$ , both sides of the chip are identical and a symmetry plane can be drawn in the middle of

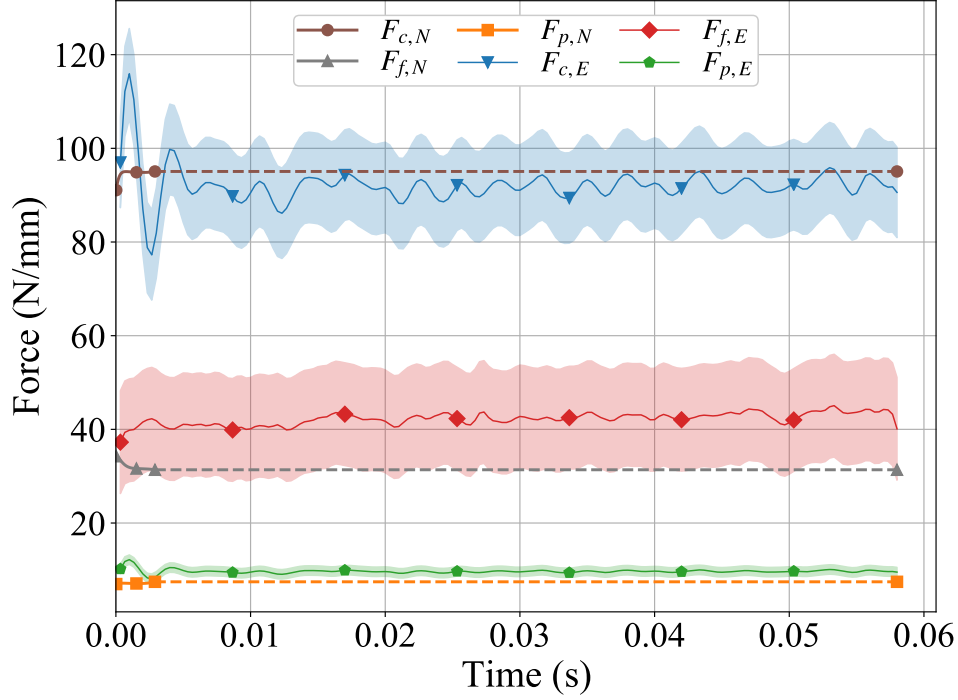


Figure 5: Temporal evolutions of experimental (E) and numerical (N) forces at  $\lambda_s = 6^\circ$ ,  $v_c = 10 \text{ m/min}$  and  $h = 40 \mu\text{m}$  with dispersion around average experimental values (linear extrapolation of numerical values in dashed)

the workpiece (Figure 7 (a)). On the other hand, for an inclination of the cutting edge of  $6^\circ$ , the chip is no longer aligned with the workpiece. The chip bends to one side due to the orientation of the tool and symmetry is lost in both the geometry and the thermal and mechanical fields, as shown in figure 7 (b). This produces helical chips for the inclination angle of  $6^\circ$  as in the experiments. Figure 8 shows the variation of the chip thickness across its width: it is thicker in the middle (i.e., the body of the chip) than on its sides. This underlines the importance of 3D modelling, even for the orthogonal cutting configuration as highlighted earlier [24]. The 3D modelling also allows reproducing the lateral flow that occurs in the experiments for both values of cutting edge inclination (Figure 6), unlike a 2D model [23–25]. Although this leads to higher computation times, future cutting models should be in 3D, even when orthogonal cutting is considered. In this



case, it is recommended to take advantage of the symmetry of the configuration to reduce the computation time. This simplification has not been included in this study to avoid any difference in the FE models between the 2 inclinations of the cutting edge.

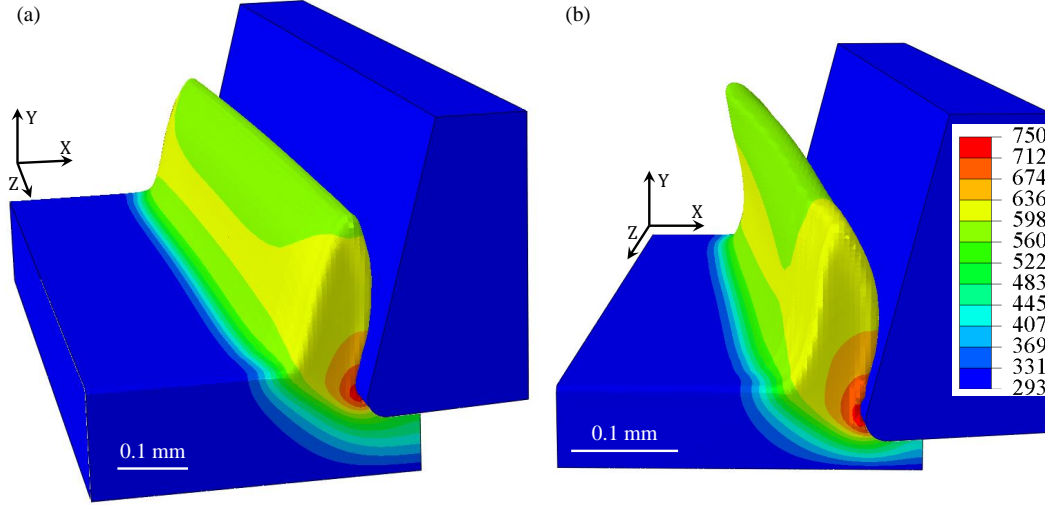


Figure 6: Temperature contours (in K) of the numerical chip after 1.5 ms at  $v_c = 10$  m/min,  $h = 40$   $\mu$ m and (a)  $\lambda_s = 0^\circ$ , (b)  $\lambda_s = 6^\circ$

Average values of the experimental forces and their dispersion are shown in Figures 9 to 13 together with the average numerical values. Passive force values are of course only plotted for  $\lambda_s = 6^\circ$  as they are equal to zero when  $\lambda_s = 0^\circ$ .

The increase in cutting force with uncut chip thickness is clearly observed in Figures 9 and 10 for both experimental and numerical results at the 2 inclination angles, as well as the decrease in force with increasing cutting speed. This shows that temperature softening dominates strain rate hardening for Ti6Al4V and is accurately modelled. Increasing the inclination angle from  $0^\circ$  to  $6^\circ$  slightly reduces the cutting force; this is well captured by the model. For cutting speeds of 20–40 m/min and an inclination angle of  $0^\circ$ ,  $F_c$  is almost constant with cutting speed for uncut chip thicknesses of 40  $\mu$ m and 60  $\mu$ m, while it decreases slightly for 80  $\mu$ m; this small stabilization is less marked for the model.

An increase in the deviation around the average value with the cutting speed is noted for values above 10 m/min. All numerical values are within 95 % confidence of the experiments (35 of the 36 conditions are within 68 % confidence). The average difference with the experiments is 4 %, which is remarkable, also

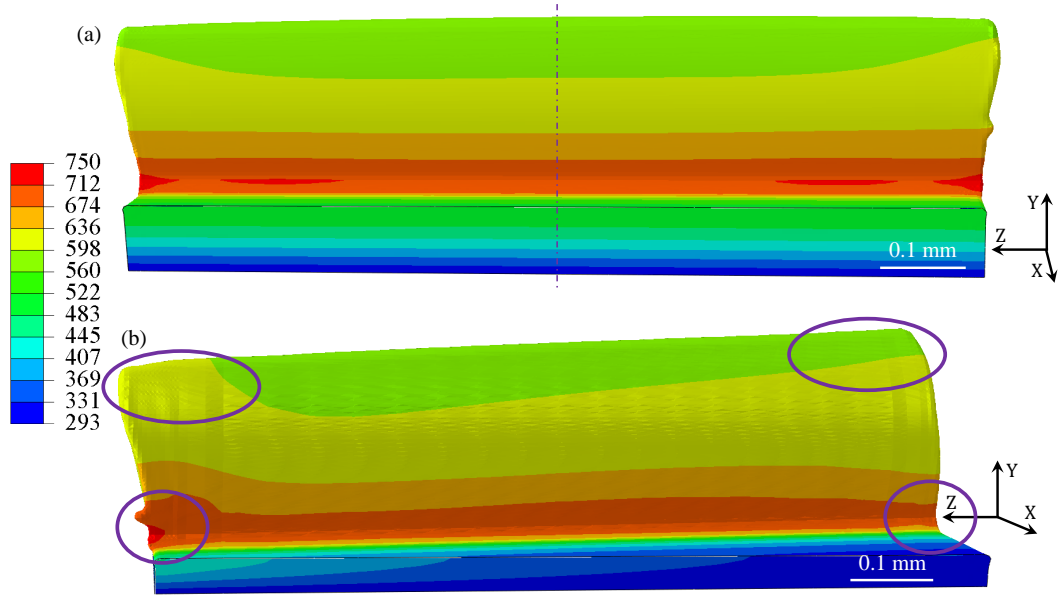


Figure 7: Temperature contours (in K) of the back of the numerical chip (tool is removed) after 1.5 ms at  $v_c = 10$  m/min,  $h = 40$   $\mu$ m and (a)  $\lambda_s = 0^\circ$ , (b)  $\lambda_s = 6^\circ$

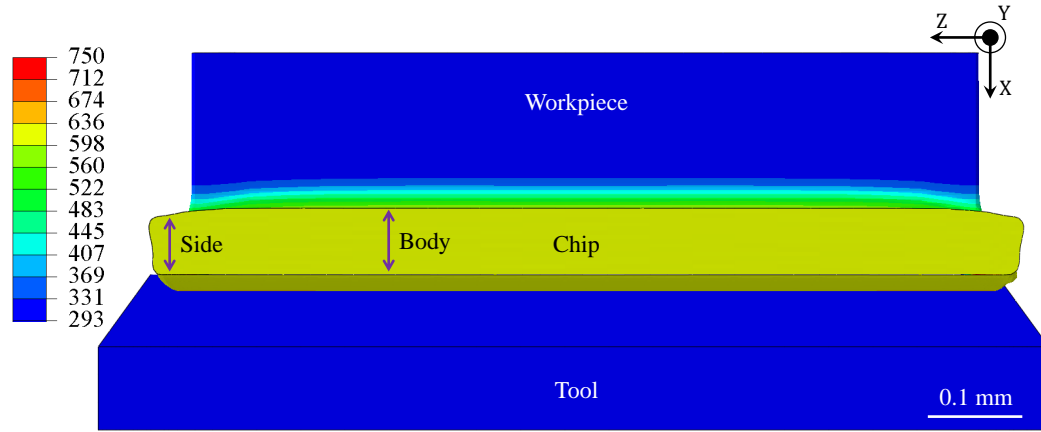


Figure 8: Temperature contours (in K) of the top of the numerical chip after 1.5 ms at  $v_c = 10$  m/min,  $h = 40$   $\mu$ m and  $\lambda_s = 0^\circ$

353 considering the wide range of cutting conditions considered and the absence of  
 354 model tuning. This underlines the predictive ability and accuracy of the FE model  
 355 for both inclination angles.

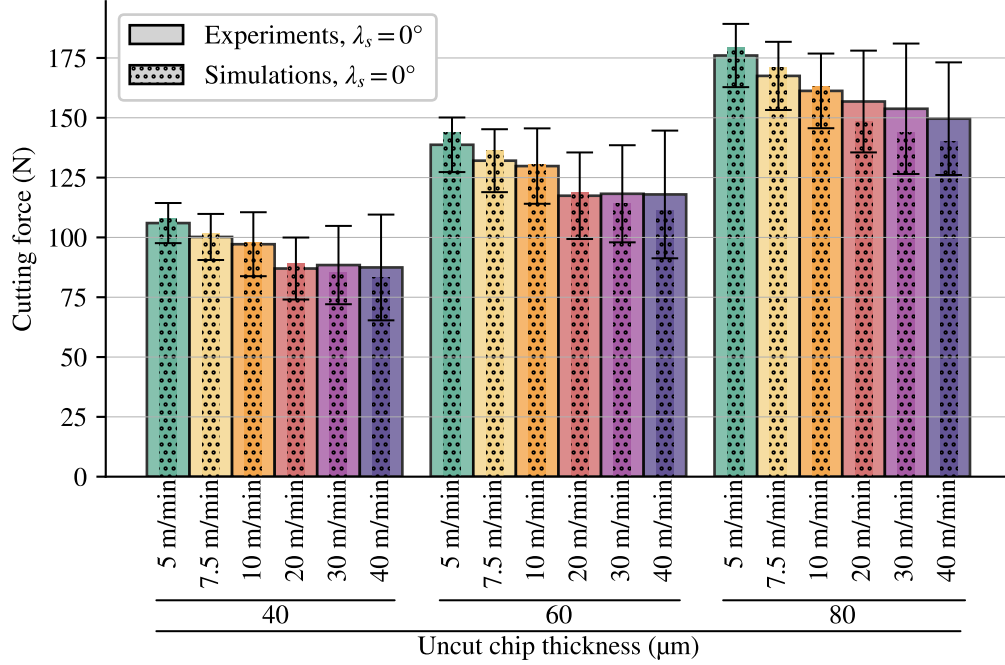


Figure 9: Comparison of experimental and numerical cutting forces at the cutting edge inclination of  $0^\circ$  for the 3 uncut chip thicknesses and the 6 cutting speeds

356 Figures 11 and 12 show the results for the feed force, where the two clearest  
 357 trends for the experiments are its decrease with the inclination angle and its in-  
 358 crease with the uncut chip thickness (even though it is lower than expected). For  
 359  $80\mu\text{m}$ ,  $F_f$  decreases overall with  $v_c$  in the experiments. For  $40\mu\text{m}$  and  $60\mu\text{m}$ , the  
 360 force decreases at lower  $v_c$ , then increases for  $0^\circ$ , while a decrease is observed at  
 361 all  $v_c$  for  $6^\circ$  (the experimental dispersion is high for both inclination angles, but the  
 362 average trend with cutting speed is clear at  $6^\circ$ , not at  $0^\circ$ ). For the numerical values,  
 363 the overall trend is the same for the 3 uncut chip thicknesses and the two inclina-  
 364 tion angles: a decrease for the lowest values of  $v_c$  and then an increase. It should  
 365 be noted that the numerical model does not correctly handle the trends of the feed  
 366 forces: as Figure 12 clearly shows, the numerical forces have an overall increas-  
 367 ing trend with the cutting speed, while their average value mainly decreases when  
 368 the uncut chip thickness increases. The differences between the average numeri-  
 369 cal and experimental values increase with the uncut chip thickness: the forces are  
 370 closer at  $40\mu\text{m}$  than at  $80\mu\text{m}$ . The numerical values are generally not within the  
 371 95 % confidence interval (they do not clearly change with the cutting conditions).

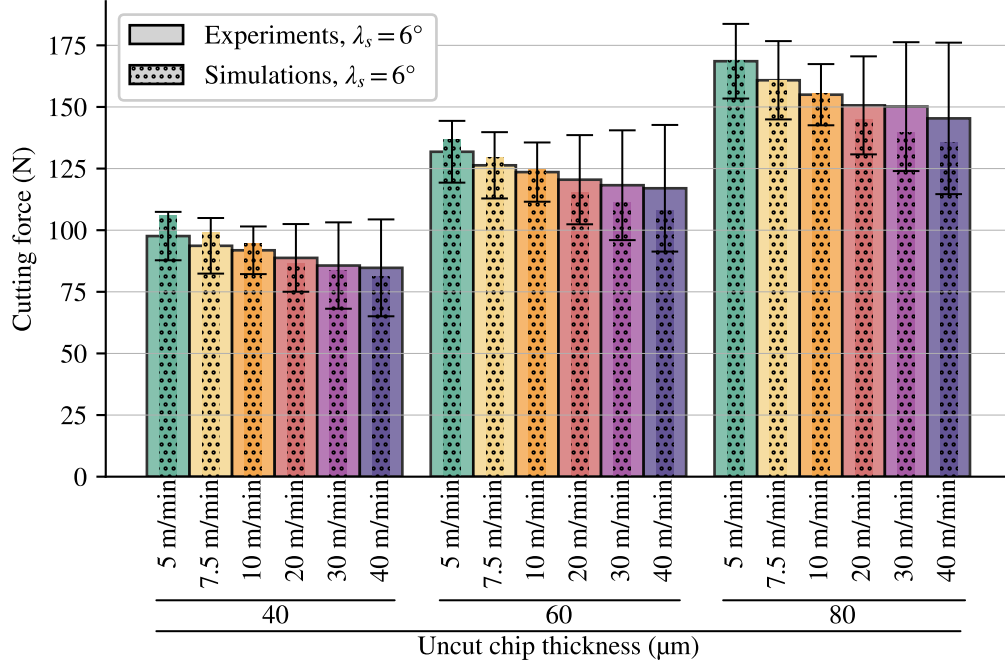


Figure 10: Comparison of experimental and numerical cutting forces at the cutting edge inclination of  $6^\circ$  for the 3 uncut chip thicknesses and the 6 cutting speeds

372 Coupled with the differences in trends, this shows that  $F_f$  is less well modelled  
373 (the average difference is 39 %) than  $F_c$  as usual in FE modelling of the cutting  
374 process and even more so in 3D [27]. The influence of the uncut chip thickness  
375 on the feed force should therefore be improved. The parameters of the material  
376 model are known to have an impact on the forces (and on the chip morphology)  
377 [15, 35]. The friction model should also be improved to strengthen the results  
378 [27].

379 The passive force is non-zero for the inclination angle of  $6^\circ$  (Figure 13). Like  
380 the cutting force, it increases with the uncut chip thickness and decreases with  
381 the cutting speed. The comparison with experiments is broadly the same as for  
382  $F_c$ , except for a greater difference in the magnitude of  $F_p$  (the average difference  
383 is 26 %, but it is small in absolute terms – less than 5 N). Most of the numerical  
384 values do not fall within the experimental 95 % confidence interval. A lower mag-  
385 nitude of the passive force from the simulation than from the experiments with  
386 the correct trends when the cutting conditions change was also observed by Hardt  
387 and Bergs [27]. The differences were mainly attributed to differences in cutting

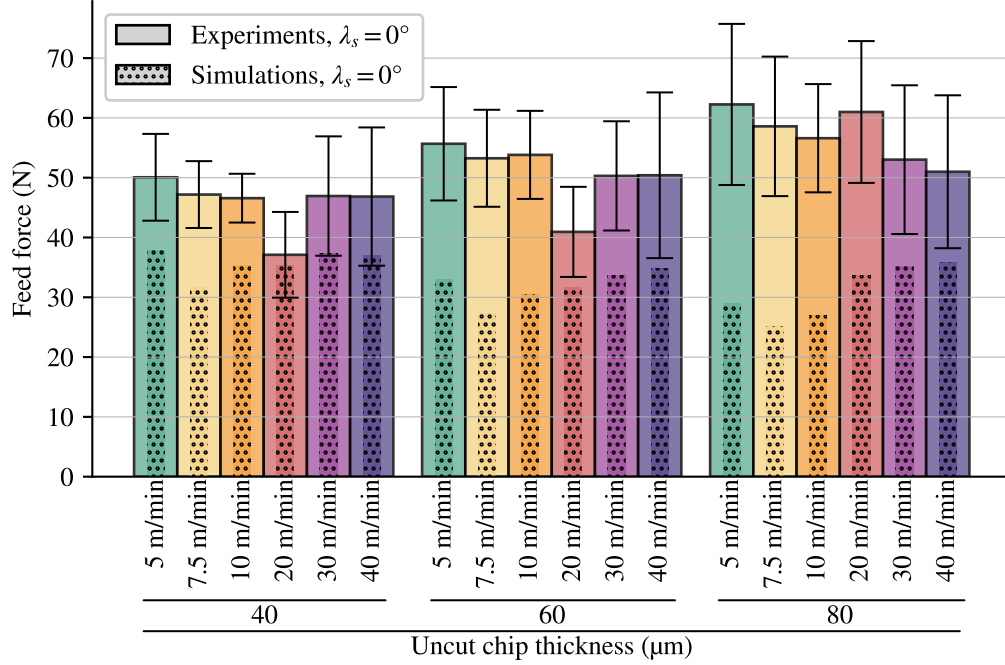


Figure 11: Comparison of experimental and numerical feed forces at the cutting edge inclination of  $0^\circ$  for the 3 uncut chip thicknesses and the 6 cutting speeds

edge radius, friction modelling and material model. In this work, the impact of the cutting edge radius can be neglected as it is the same in the model as in the experiments.

As far as the chip morphology is concerned, all chips are continuous. For both the simulation and the experiments, the chip thickness ratio,  $\lambda_h$  :

$$\lambda_h = \frac{h'}{h} \quad (13)$$

with  $h$  the uncut chip thickness and  $h'$  the chip thickness, is almost independent of the uncut chip thickness (Figures 14 and 15). It is slightly reduced from  $\lambda_s = 0^\circ$  to  $\lambda_s = 6^\circ$ , which means that the chip thickness decreases with the inclination angle. This influence is underestimated by the model: the reduction of  $\lambda_h$  is smaller than in the experiments. The average difference between the experimental and numerical  $\lambda_h$  is 17 % over the whole range of cutting conditions. The chip thickness ratio decreases with cutting speed due to the reduction in friction, which is correctly accounted for by the model. As with the feed force, the results should be improved

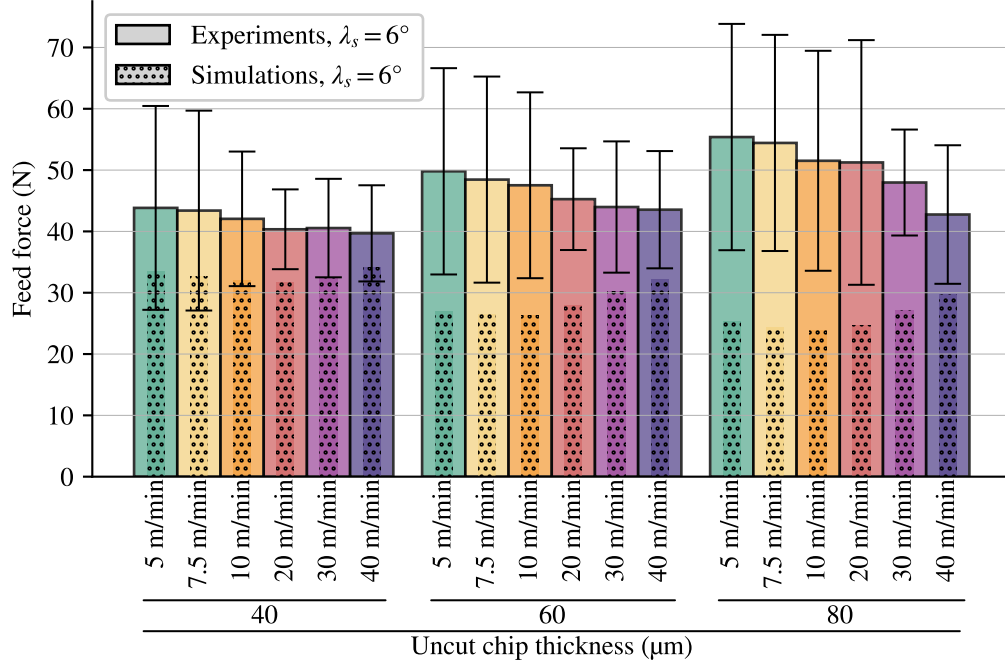


Figure 12: Comparison of experimental and numerical feed forces at the cutting edge inclination of  $6^\circ$  for the 3 uncut chip thicknesses and the 6 cutting speeds

by more complex friction models and a set of material parameters for which the identification includes forces and chip thickness: [15].

The differences calculated according to the equation (12) are presented in Table 6 to provide a quantitative overview of the results. The cutting force is the best modelled quantity as observed in the literature. This result was to be expected as the parameter set of the material model was selected mainly due to its good approximation of the cutting force [35]. As this selection was made with a 2D model, the results show the ability of the model to correctly handle the third (passive) force. Based on the average differences, the performance of the model is very close for the cutting and feed forces for both cutting edge inclinations, although a small degradation (1 % and 2 %, respectively) is noted for  $6^\circ$ . This degradation is more important (7 %) for the chip thickness ratio and must be linked to the difference in passive force. Indeed, the chip thickness and out-of-plane force models are deeply linked. Improving the friction at the tool-workpiece interface should be a key point. It should be noted that the chip thickness is very well modelled under certain cutting conditions with a minimum difference of 2 %. The difference

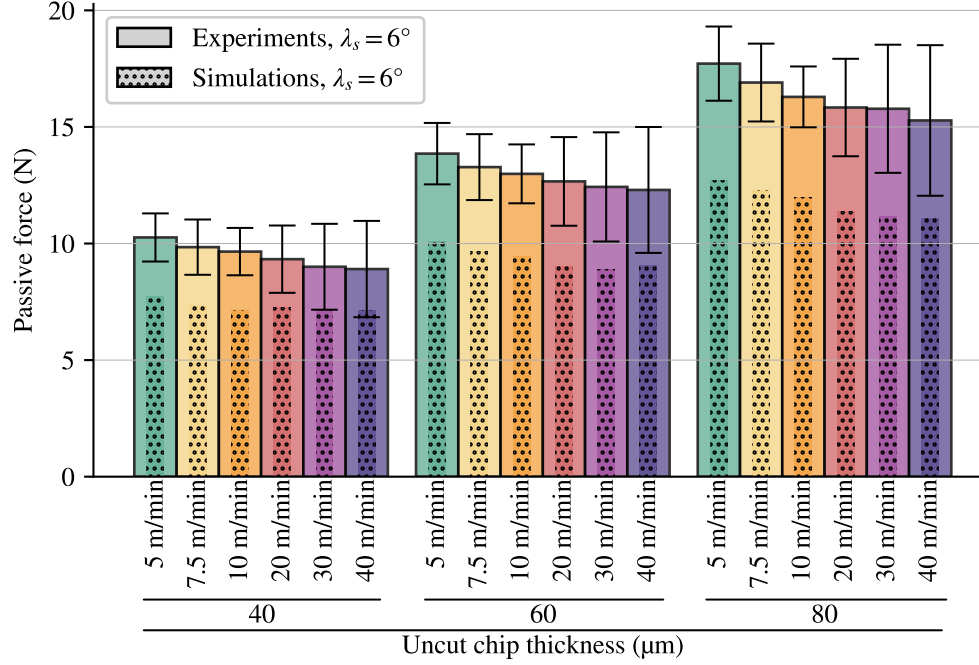


Figure 13: Comparison of experimental and numerical passive forces at the cutting edge inclination of  $6^\circ$  for the 3 uncut chip thicknesses and the 6 cutting speeds

is larger for the feed force than for the passive force, a trend opposite to that of Hardt and Bergs [27]. The average and range (min – max) of the differences are larger for the feed force. The smaller range of the passive force confirms a shift for all cutting conditions, similar to the results of Hardt and Bergs [27]. Again, the friction modelling should be the first aspect of the model to be improved in future developments.

## 5. Conclusions

An experimental and numerical study of the orthogonal and oblique free cutting of Ti6Al4V was carried out for a wide range of cutting conditions using an ANN-based flow law. The following main conclusions are drawn:

- The experimental study was carried out with the same set-up in free orthogonal and free oblique cutting for the titanium alloy Ti6Al4V (the only change is the cutting edge inclination). This is a reference to evaluate the

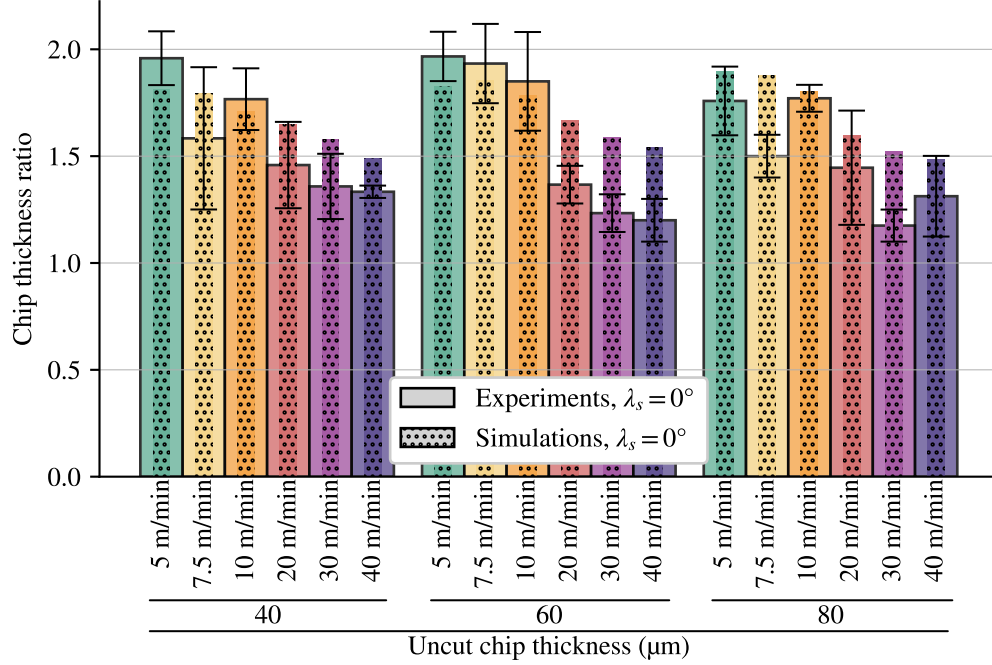


Figure 14: Comparison of experimental and numerical chip thickness ratios at the cutting edge inclination of  $0^\circ$  for the 3 uncut chip thicknesses and the 6 cutting speeds

Table 6: Synthetic quantitative overview of the results: differences between the experimental and the numerical results (average difference for each cutting edge inclination, and maximal, minimal and average differences for all the conditions) for the cutting force,  $\Delta F_c$ , the feed force,  $\Delta F_f$ , the passive force,  $\Delta F_p$ , and the chip thickness ratio,  $\Delta \lambda_h$

Difference	$\Delta F_c$ (%)	$\Delta F_f$ (%)	$\Delta F_p$ (%)	$\Delta \lambda_h$ (%)
Average $\lambda_s = 0^\circ$	3	38	–	14
Average $\lambda_s = 6^\circ$	4	40	26	21
Max. global	10	60	29	38
Min. global	1	10	19	2
Average global	4	39	26	17

performance of the FE 3D model introducing an ANN-based flow law developed under the same conditions. An unpreviously seen wide range of cutting conditions, 36, is considered, including 2 cutting edge inclinations.



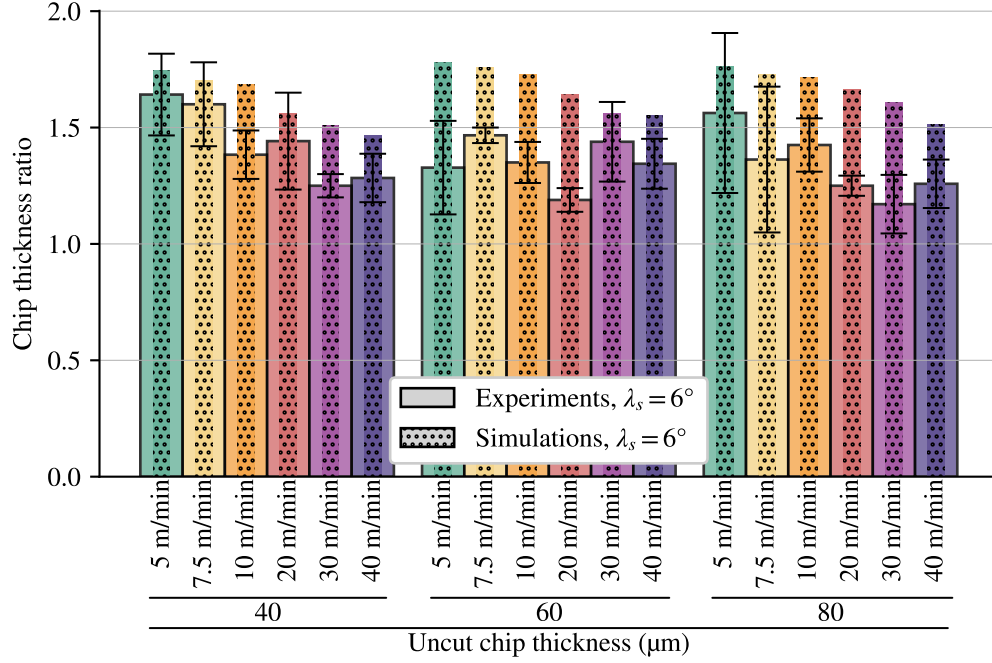


Figure 15: Comparison of experimental and numerical chip thickness ratios at the cutting edge inclination of  $6^\circ$  for the 3 uncut chip thicknesses and the 6 cutting speeds

- A major novelty of this work is the accurate evaluation of the fundamental variables and their trends in 3D, without the need to adjust the numerical parameters and the model characteristics when the cutting conditions and the inclination angle are changed significantly. The mere fact of changing the inclination angle from free orthogonal cutting to oblique cutting while maintaining the quality of the results has no equivalent in the current literature, especially since no studies (experimental or numerical) on free oblique cutting are available.
- Taking into account the material's flow law by means of a neural network makes it possible to overcome the limitations of conventional flow laws and to reduce the approximations associated with the establishment of an analytical formulation of the flow law as conventionally adopted. The numerical model is then able to better reproduce the real behaviour of the material and to take into account thermomechanical transformations which are sources of non-linearities, difficult to take into account with an analytical flow law

model. Current work, using a Gleeble thermomechanical simulator, on the behaviour of a modified carbon alloy AISI P20 shows the advantages of this approach compared to models in the literature such as Johnson-Cook, Zerilli-Armstrong [5] or Hansel-Spittel [46], insofar as one is then able to better reproduce more complex material behaviours.

- The cutting force is the best modelled quantity with an average difference of 4 % with the experiments. Chip thickness ratio and passive force show a larger deviation from the experiments (17 % and 26 %, respectively), but their trends as the cutting conditions change are accurate. This is in line with the expected results provided by a predictive model. The deviation for feed force is higher (39 %), and opposite trends compared to the experimental reference are observed. The lack of influence of uncut chip thickness on friction in the model seems to be one of the aspects to be included as a priority in future work. The model is found to handle the occurrence of the third force, out of plane, well without significant degradation of the results.
- The predictive capabilities of the model make it suitable for the development of straight-edged tools, for example. This work also demonstrates the ability to model material behaviour with ANN and opens up possibilities in this promising direction.

## 6. Statements & Declarations

### Funding

The authors declare that this research received no external funding.

### Competing Interests

The authors have no relevant financial or non-financial interests to disclose.

### Author Contributions

François Ducobu contributed to Data curation, Formal analysis, Investigation, Methodology, Software, Supervision, Validation, Visualization, Writing – original draft and review & editing (focussing on non ANN-related aspects). Olivier Pantalé contributed to Data curation, Formal analysis, Investigation, Methodology, Software, Validation, Visualization, Writing – original draft and review & editing (focussing on ANN-related aspects). Bert Lauwers contributed to Supervision and Writing – review & editing. All authors read and approved the final manuscript.

## References

- [1] P. J. Arrazola, T. Özel, D. Umbrello, M. Davies, I. S. Jawahir, Recent advances in modelling of metal machining processes, *CIRP Annals* 62 (2013) 695–718.
- [2] S. N. Melkote, W. Grzesik, J. Outeiro, J. Rech, V. Schulze, H. Attia, P.-J. Arrazola, R. M'Saoubi, C. Saldana, Advances in material and friction data for modelling of metal machining, *CIRP Annals* 66 (2017) 731–754.
- [3] G. Johnson, W. Cook, A constitutive model and data for metals subjected to large strains, high strain rates and high temperatures, in: *Proc. 7th International Symposium on Ballistics*, volume 21, The Hague, The Netherlands, pp. 541–547.
- [4] M. Calamaz, D. Coupard, F. Girod, A new material model for 2D numerical simulation of serrated chip formation when machining titanium alloy Ti–6Al–4V, *International Journal of Machine Tools and Manufacture* 48 (2008) 275–288.
- [5] M. M. Gurusamy, B. C. Rao, On the performance of modified Zerilli-Armstrong constitutive model in simulating the metal-cutting process, *Journal of Manufacturing Processes* 28 (2017) 253–265.
- [6] T. Özel, T. Altan, Determination of workpiece flow stress and friction at the chip–tool contact for high-speed cutting, *Int J Mach Tools Manuf* 40 (2000) 133–152.
- [7] A. Shrot, M. Bäker, Determination of Johnson–Cook parameters from machining simulations, *Comput Mater Sci* 52 (2012) 298–304.
- [8] F. Klocke, D. Lung, S. Buchkremer, I. S. Jawahir, From Orthogonal Cutting Experiments towards Easy-to-Implement and Accurate Flow Stress Data, *Materials and Manufacturing Processes* 28 (2013) 1222–1227.
- [9] P. Bosetti, C. Maximiliano Giorgio Bort, S. Bruschi, Identification of Johnson–Cook and Tresca's Parameters for Numerical Modeling of AISI-304 Machining Processes, *J Manuf Sci Eng* 135 (2013).
- [10] B. Denkena, T. Grove, M. A. Dittrich, D. Niederwestberg, M. Lahres, Inverse Determination of Constitutive Equations and Cutting Force Modelling

- 514 for Complex Tools Using Oxley's Predictive Machining Theory, *Procedia*  
515 *CIRP* 31 (2015) 405–410.
- 516 [11] T. Bergs, M. Hardt, D. Schraknepper, Determination of Johnson-Cook ma-  
517 terial model parameters for AISI 1045 from orthogonal cutting tests using  
518 the Downhill-Simplex algorithm, *Procedia Manuf* 48 (2020) 541–552.
- 519 [12] M. Hardt, D. Schraknepper, T. Bergs, Investigations on the Application of  
520 the Downhill-Simplex-Algorithm to the Inverse Determination of Material  
521 Model Parameters for FE-Machining Simulations, *Simulation Modelling*  
522 *Practice and Theory* 107 (2021) 102214.
- 523 [13] B. Stampfer, G. González, E. Segebade, M. Gerstenmeyer, V. Schulze, Ma-  
524 terial parameter optimization for orthogonal cutting simulations of AISI4140  
525 at various tempering conditions, *Procedia CIRP* 102 (2021) 198–203.
- 526 [14] M. Hardt, D. Jayaramaiah, T. Bergs, On the Application of the Particle  
527 Swarm Optimization to the Inverse Determination of Material Model Pa-  
528 rameters for Cutting Simulations, *Modelling 2* (2021) 129–148.
- 529 [15] N. Kugalur Palanisamy, E. Rivière Lorphèvre, M. Gobert, G. Briffoteaux,  
530 D. Tuytens, P.-J. Arrazola, F. Ducobu, Identification of the Parameter Val-  
531 ues of the Constitutive and Friction Models in Machining Using EGO Algo-  
532 rithm: Application to Ti6Al4V, *Metals* 12 (2022) 976.
- 533 [16] F. Ducobu, N. K. Palanisamy, P.-J. Arrazola, E. Rivière-Lorphèvre, Appli-  
534 cation of material constitutive and friction models parameters identified with  
535 AI and ALE to a CEL orthogonal cutting model, *Procedia CIRP* 117 (2023)  
536 311–316.
- 537 [17] M. B. Gorji, M. Mozaffar, J. N. Heidenreich, J. Cao, D. Mohr, On the po-  
538 tential of recurrent neural networks for modeling path dependent plasticity,  
539 *Journal of the Mechanics and Physics of Solids* 143 (2020) 103972.
- 540 [18] M. R. Jamli, N. M. Farid, The sustainability of neural network applications  
541 within finite element analysis in sheet metal forming: A review, *Measure-*  
542 *ment* 138 (2019) 446–460.
- 543 [19] P. Tize Mha, P. Dhondapure, M. Jahazi, A. Tongne, O. Pantalé, Interpolation  
544 and Extrapolation Performance Measurement of Analytical and ANN-Based

- 545 Flow Laws for Hot Deformation Behavior of Medium Carbon Steel, *Metals*  
546 13 (2023) 633.
- 547 [20] O. Pantalé, Development and Implementation of an ANN Based Flow Law  
548 for Numerical Simulations of Thermo-Mechanical Processes at High Tem-  
549 peratures in FEM Software, *Algorithms* 16 (2023) 56.
- 550 [21] P. Tize Mha, P. Dhondapure, M. Jahazi, A. Tongne, O. Pantalé, Artificial  
551 Neural Network-Based Critical Conditions for the Dynamic Recrystalliza-  
552 tion of Medium Carbon Steel and Application, *Metals* 13 (2023) 1746.
- 553 [22] F. Ducobu, E. Rivière-Lorphèvre, E. Filippi, Application of the Coupled  
554 Eulerian-Lagrangian (CEL) method to the modeling of orthogonal cutting,  
555 *Eur J Mech A Solids* 59 (2016) 58–66.
- 556 [23] X. Xu, J. Outeiro, J. Zhang, B. Li, W. Zhao, Simulation of material side flow  
557 using a 3D coupled Eulerian-Lagrangian approach and a constitutive model  
558 considering the stress state, *Procedia CIRP* 102 (2021) 441–446.
- 559 [24] F. Ducobu, E. Rivière-Lorphèvre, E. Filippi, Finite element modelling of 3D  
560 orthogonal cutting experimental tests with the Coupled Eulerian-Lagrangian  
561 (CEL) formulation, *Finite Elements in Analysis and Design* 134 (2017) 27–  
562 40.
- 563 [25] D. Ambrosio, A. Tongne, V. Wagner, G. Dessein, O. Cahuc, A new damage  
564 evolution criterion for the coupled Eulerian-Lagrangian approach: Applica-  
565 tion to three-dimensional numerical simulation of segmented chip formation  
566 mechanisms in orthogonal cutting, *Journal of Manufacturing Processes* 73  
567 (2022) 149–163.
- 568 [26] A. Vovk, J. Sölter, B. Karpuschewski, Finite element simulations of the  
569 material loads and residual stresses in milling utilizing the CEL method,  
570 *Procedia CIRP* 87 (2020) 539–544.
- 571 [27] M. Hardt, T. Bergs, Three Dimensional Numerical Modeling of Face Turn-  
572 ing Using the Coupled-Eulerian-Lagrangian Formulation, *Procedia CIRP*  
573 102 (2021) 162–167.
- 574 [28] M. Agmell, V. Bushlya, S. V. A. Laakso, A. Ahadi, J.-E. Ståhl, Development  
575 of a simulation model to study tool loads in pcBN when machining AISI  
576 316L, *Int J Adv Manuf Technol* 96 (2018) 2853–2865.

- 577 [29] M. Abouridouane, T. Bergs, D. Schraknepper, G. Wirtz, Friction behavior  
578 in metal cutting: Modeling and simulation, *Procedia CIRP* 102 (2021) 405–  
579 410.
- 580 [30] F. Ducobu, E. Rivière-Lorphèvre, E. Filippi, Experimental contribution to  
581 the study of the Ti6Al4V chip formation in orthogonal cutting on a milling  
582 machine, *Int J Mater Form* 8 (2015) 455–468.
- 583 [31] A. Sela, G. Ortiz-de-Zarate, D. Soler, G. Germain, P. Aristimuño, P. J. Arra-  
584 zola, Measurement of plastic strain and plastic strain rate during orthogonal  
585 cutting for Ti-6Al-4V, *International Journal of Mechanical Sciences* 198  
586 (2021) 106397.
- 587 [32] M. Afrasiabi, J. Saelzer, S. Berger, I. Iovkov, H. Klippel, M. Röthlin,  
588 A. Zabel, D. Biermann, K. Wegener, A Numerical-Experimental Study on  
589 Orthogonal Cutting of AISI 1045 Steel and Ti6Al4V Alloy: SPH and FEM  
590 Modeling with Newly Identified Friction Coefficients, *Metals* 11 (2021)  
591 1683.
- 592 [33] O. Pantalé, P. Tize Mha, A. Tongne, Efficient implementation of non-linear  
593 flow law using neural network into the Abaqus Explicit FEM code, *Finite  
594 Elements in Analysis and Design* 198 (2022) 103647.
- 595 [34] S. Seo, O. Min, H. Yang, Constitutive equation for Ti–6Al–4V at high tem-  
596 peratures measured using the SHPB technique, *Int J Impact Eng* 31 (2005)  
597 735–754.
- 598 [35] F. Ducobu, E. Rivière-Lorphèvre, E. Filippi, On the importance of the choice  
599 of the parameters of the Johnson-Cook constitutive model and their influence  
600 on the results of a Ti6Al4V orthogonal cutting model, *Int J Mech Sci* 122  
601 (2017) 143–155.
- 602 [36] GRANTA EduPack 2020, Granta Design Limited, 2020.
- 603 [37] N. Milošević, I. Aleksic, Thermophysical properties of solid phase Ti-6Al-  
604 4V alloy over a wide temperature range (2012).
- 605 [38] J. Rech, P. J. Arrazola, C. Claudin, C. Courbon, F. Pusavec, J. Kopac, Char-  
606 acterisation of friction and heat partition coefficients at the tool-work mate-  
607 rial interface in cutting, *CIRP Annals* 62 (2013) 79–82.

- [39] O. Pantalé, Coefficients of an ANN constitutive flow law of a Ti6-Al-4V material for dynamic applications, Zenodo (2022).
- [40] L. Wang, H. Long, Investigation of material deformation in multi-pass conventional metal spinning, *Materials & Design* 32 (2011) 2891–2899.
- [41] F. Ducobu, E. Rivière-Lorphèvre, E. Filippi, On the introduction of adaptive mass scaling in a finite element model of Ti6Al4V orthogonal cutting, *Simulation Modelling Practice and Theory* 53 (2015) 1–14.
- [42] M. Sima, T. Özel, Modified material constitutive models for serrated chip formation simulations and experimental validation in machining of titanium alloy Ti–6Al–4V, *International Journal of Machine Tools and Manufacture* 50 (2010) 943–960.
- [43] F. Ducobu, E. Rivière-Lorphèvre, E. Filippi, Material constitutive model and chip separation criterion influence on the modeling of Ti6Al4V machining with experimental validation in strictly orthogonal cutting condition, *International Journal of Mechanical Sciences* 107 (2016) 136–149.
- [44] Y. Karpas, Temperature dependent flow softening of titanium alloy Ti6Al4V: An investigation using finite element simulation of machining, *Journal of Materials Processing Technology* 211 (2011) 737–749.
- [45] Y. C. Zhang, T. Mabrouki, D. Nelias, Y. D. Gong, Chip formation in orthogonal cutting considering interface limiting shear stress and damage evolution based on fracture energy approach, *Finite Elements in Analysis and Design* 47 (2011) 850–863.
- [46] K. Chadha, D. Shahriari, M. Jahazi, An Approach to Develop Hansel–Spittel Constitutive Equation during Ingot Breakdown Operation of Low Alloy Steels, in: M. Muruganant, A. Chirazi, B. Raj (Eds.), *Frontiers in Materials Processing, Applications, Research and Technology*, Springer, Singapore, 2018, pp. 239–246.

## Appendix A. Coefficients of the ANN 3-9-7-1-sig

In this appendix, we present the values obtained after the training phase of an ANN containing 9 neurons in the first hidden layer and 7 neurons in the second hidden layer. Conforming to [33], this one is referred ANN-3-9-7-1-sig. The

639 training of the neural network was performed using a dataset containing 3430  
640 data points defined by:

- 641 • 70 equidistant values for  $\varepsilon^p \in [0, 3]$ , so that  $[\varepsilon^p]_{min} = 0$  and  $[\varepsilon^p]_{max} = 3$ .
- 642 • 7 plastic strain rates  $\dot{\varepsilon}^p \in [1/s, 10/s, 50/s, 500/s, 5000/s, 50\,000/s, 500\,000/s]$ ,  
643 so that  $[\ln(\dot{\varepsilon}^p)]_{min} = 0$  and  $[\ln(\dot{\varepsilon}^p)]_{max} = 13.12236$ .
- 644 • 7 temperatures  $T \in [293\text{ K}, 400\text{ K}, 500\text{ K}, 700\text{ K}, 900\text{ K}, 1200\text{ K}, 1500\text{ K}]$ , so  
645 that  $[T]_{min} = 293\text{ K}$  and  $[T]_{max} = 1500\text{ K}$ .

646 Stresses in the training dataset ranges from  $[\sigma^y]_{min} = 171.4\text{ MPa}$  to  $[\sigma^y]_{max} =$   
647  $2606.1\text{ MPa}$ . The results of the training process are given here after for the ANN  
648 quantities  $\mathbf{W}_1$ ,  $\mathbf{W}_2$ ,  $\vec{w}$ ,  $\vec{b}_1$ ,  $\vec{b}_2$  and  $b$ . The weight matrix for the first hidden layer  
649  $\mathbf{W}_1$  is a  $9 \times 3$  matrix:

$$\mathbf{W}_1 = \begin{bmatrix} -0.87229 & -0.47675 & -1.50771 \\ -0.95762 & -0.25619 & 1.65222 \\ -10.61660 & 0.22003 & -0.11539 \\ 3.67883 & 0.37146 & -1.51069 \\ -63.39468 & 0.15466 & -0.95431 \\ 0.54807 & 0.25959 & -5.44355 \\ -1.33883 & 0.36089 & -1.66735 \\ -0.68125 & 1.02121 & 0.34242 \\ 0.08740 & 0.18764 & -41.32542 \end{bmatrix}$$

650 The weight matrix for the second hidden layer  $\mathbf{W}_2$  is a  $7 \times 9$  matrix:

$$\mathbf{W}_2^T = \begin{bmatrix} 1.66285 & -0.59645 & -3.17333 & 0.20706 & 1.18760 & 2.01250 & -0.82147 \\ -0.26237 & -2.50330 & -1.45941 & -1.59833 & 4.05169 & -1.21146 & 1.05610 \\ -0.12958 & 0.67119 & -5.85989 & -2.55061 & 4.85245 & 4.31876 & 3.24070 \\ -2.12890 & 0.68296 & 0.71183 & 0.81706 & -0.09405 & 0.34919 & -1.41223 \\ 2.33631 & -0.08089 & 14.65789 & 0.12531 & 23.66363 & 2.55872 & 2.15338 \\ 0.11567 & 1.77629 & -1.80448 & 0.77825 & -1.58254 & 1.90442 & 1.23152 \\ 1.49265 & 0.41821 & -3.53803 & -0.48705 & -0.23671 & 0.75887 & -0.37441 \\ 0.95990 & 0.69041 & 0.43870 & 0.28393 & -1.40101 & -0.64569 & -0.38964 \\ 5.89937 & -0.13015 & 2.99264 & 1.78534 & -3.90189 & 1.17494 & -3.78854 \end{bmatrix}$$

651 The weight vector for the output layer  $\vec{w}$  is a 7 components vector:



$$\vec{w} = \begin{bmatrix} 0.34701 \\ 1.42079 \\ -0.96564 \\ 0.62467 \\ -0.56322 \\ 0.40960 \\ -0.42810 \end{bmatrix}$$

652 The biases of the first hidden layer  $\vec{b}_1$  is a 9 components vector:

$$\vec{b}_1 = \begin{bmatrix} 2.57141 \\ 0.22673 \\ -1.16985 \\ -0.11246 \\ -0.82210 \\ -2.13264 \\ 0.78794 \\ 1.20434 \\ -3.48681 \end{bmatrix}$$

653 The biases of the second hidden layer  $\vec{b}_2$  is a 7 components vector:

$$\vec{b}_2 = \begin{bmatrix} -0.36566 \\ -1.14445 \\ -0.79065 \\ -0.50670 \\ 1.30136 \\ 0.04521 \\ -0.29995 \end{bmatrix}$$

654 The bias of the output layer  $b$  is a scalar:

$$b = 0.04213$$

655 The corresponding coefficients for the other networks identified during this  
656 work (ANN-3-11-7-1-sig, ANN-3-13-7-1-sig, ANN-3-15-7-1-sig and ANN-3-17-  
657 7-1-sig) can be found in [39].